Temperature invariance of InN electron accumulation

L. F. J. Piper, T. D. Veal, I. Mahboob, and C. F. McConville*
Department of Physics, University of Warwick, Coventry CV4 7AL, United Kingdom

Hai Lu and W. J. Schaff
Department of Electrical and Computer Engineering, Cornell University, Ithaca, New York 14853, USA
(Received 8 April 2004; published 30 September 2004)

The temperature dependence of the electron accumulation at clean InN(0001)-(1×1) surfaces has been investigated by high-resolution electron-energy-loss spectroscopy. Semiclassical dielectric theory simulations of the energy-loss spectra at 295 K and 565 K along with solutions to the Poisson equation enable carrier profiles of the near-surface region to be determined. These measurements reveal similar electron accumulation for both temperatures. The surface-state density, N_{ss}, and the surface Fermi level, E_{FS}, were found to be independent of temperature, with $N_{ss}\sim2.4\times10^{13}$ cm^{-2} and $E_{FS}\sim1.5$ eV above the valence-band maximum. The slight difference in the carrier profiles between the two temperatures can be accounted for by the change in the electron screening length. This is a consequence of the reduction in the band gap that results in a decrease in the electron effective mass with increasing temperature.

DOI: 10.1103/PhysRevB.70.115333 PACS number(s): 73.20.Mf, 73.61.Ey, 71.20.Nr

I. INTRODUCTION

It has been reported recently that InN surfaces naturally exhibit electron accumulation.[1,2] This is consistent with band-structure calculations, which have revealed an unusually low conduction-band minimum at the Γ point.[3,4] This minimum allows donor-type surface states to exist in the conduction band, into which they emit their electrons, giving rise to electron accumulation at the surface.[1,5,6]

Due to the problems encountered when attempting to grow InN layers thicker than 1 μm,[7] most of the studies so far have been carried out on thin films. Generally, single-field Hall measurements are used to determine carrier concentrations, but these measurements on thin films have been dominated by the accumulation. Therefore, such measurements provide only an average value for the carrier concentration. Multiple-field Hall measurements and the application of quantitative mobility spectrum analysis are required to account for the parallel conduction in the surface and bulk layers to obtain the true bulk sheet carrier density and mobility.[8]

An alternative approach is high-resolution electron-energy-loss spectroscopy (HREELS), a noncontact and nondestructive probing technique that can be used for studying the semiconductor space-charge region. HREELS probes the collective excitations near the surface and is capable of distinguishing between contributions from the accumulation layer and the bulk.[1,9–11] Simulations of the HREEL spectra combined with charge-profile calculations enable the surface Fermi level, band bending, and the surface-state density to be determined. Knowledge of these properties is essential in achieving a full understanding of InN and InN-based devices. However, the effects of temperature on these fundemental parameters have yet to be explored.

InN is potentially a suitable material for midinfrared detection over a wide range of temperatures. The small temperature dependence of the band gap compared to similar narrow-gap materials[12,13] results in little change in the electronic properties with temperature. Additionally, the natural electron accumulation at the surface allows good Ohmic contacts to be formed.[1,2] Both properties are beneficial for device operations, but further understanding of the surface electron accumulation is required. In this paper, we investigate the near-surface space-charge properties of InN(0001) at 295 K and 565 K.

II. EXPERIMENTAL DETAILS

Experiments were undertaken using a conventional ultrahigh-vacuum chamber equipped with low-energy electron diffraction (LEED) and HREELS (VSW Ltd., UK). Surface preparation was carried out using a TC-50 thermal cracker (Oxford Applied Research, UK). InN(0001) thin films were grown to a thickness of 1500 nm by migration-enhanced gas source molecular-beam epitaxy on top of a 200 nm GaN buffer layer. A further 200 nm AlN layer was grown between the buffer layer and the *c*-plane sapphire substrate. The InN layer was unintentionally *n*-type doped. Details of the growth can be found elsewhere.[14] Single-field Hall measurement indicated an average conduction electron density, n, of 1.83×10^{18} cm^{-3} and an average mobility of 1200 cm^2 V^{-1} s^{-1}. The polarity of the InN film was determined by coaxial impact collision ion scattering spectroscopy (CAISISS). Comparisons between experimental data and simulations of different volume ratios of (0001) and $(000\bar{1})$ domains revealed that the InN films are mainly In polarity or (0001), but with approximately 25% N polarity or $(000\bar{1})$ material.[15]

The HREELS experiments were performed using a specular scattering geometry with an incident and scattered polar angle of 45°. The HREELS spectrometer consists of two hemispherical electron energy analyzers, one used to monochromate the incident electron beam and the other to energy analyze the reflected beam. The resolution of the HREEL

spectrometer is determined by the full width at half maximum of the elastic peak, which was found to be ~13 meV.

Following insertion into the HREELS chamber, InN surface preparation was achieved *in situ* by atomic hydrogen cleaning (AHC) in order to remove the atmospheric contaminants. The more conventional method of ion bombardment and annealing (IBA) is not well suited to the preparation of InN surfaces since donor-type defects are created by IBA. This enhances the already high conduction electron density, as seen previously in InAs.[9] However the preparation of InAs using AHC has been shown not to affect the bulk electron density,[9,16] since thermal atomic hydrogen sources produce hydrogen radicals whose energies are less than 1 eV.[17] The sample was initally cleaned at 295 K for 8 kL of H_2 and then heated to 450 K for a further 8 kL of H_2. Afterwards, the sample was annealed for 1 h at 575 K. The InN(0001) samples produced a (1×1) LEED pattern after cleaning, indicating a well-ordered surface. The removal of atmospheric contaminants was confirmed by HREELS, due to the absence of vibrational modes associated with adsorbed hydrocarbons and native oxides.

III. HREEL SPECTRA

In HREELS, a monoenergetic beam of electrons impinges on the samples surface, and the scattered electrons are energy analyzed. The majority of the probing electrons are elastically scattered, giving rise to a peak at zero loss energy. Other energy-loss features in the spectra are associated with the energy exchange between the collective excitations of the conduction electrons and the lattice with the inelastically scattered electrons. Investigations of surface plasmons are useful in semiconductor materials as they provide information about the electronic properties. This is achieved by varying the probing energy of the electrons, which allows information to be obtained from the entire space-charge region.[9]

An example of normalized HREEL spectra recorded from a clean InN(0001) surface at 295 K and 565 K at two different probing energies, along with semi-classical dielectric theory simulations, is shown in Fig. 1. Two distinct features are observed in the HREEL spectra. The first loss feature at ~66 meV is assigned to Fuchs-Kliewer surface-phonon excitations.[18] The second loss feature at ~200–250 meV results from conduction-band electron plasmon excitations. Both the 295 K and 565 K data sets show a decrease in plasmon peak energy with increasing probing energy. The plasmon peak dispersion for a larger set of probing energies shows the same trend at both temperatures, as shown in Fig. 2.

The higher probing energies correspond to deeper probing depths. The variation in probing depths arises from the long-ranged electric fields associated with surface excitations. The field exponentially decays from the excitation into the vacuum in the form $\exp(-q_{\|}z)$, where $q_{\|}$ is the wave-vector transfer parallel to the surface and z is the depth of the excitation. By varying the kinetic energy of the probing electron, the inverse of the wave-vector transfer parallel is changed, thus enabling the probing depth to be varied.[10,19,20] In this case, a maximum probing depth of 200 Å is achieved. Figures 1 and 2 can then be understood in terms of a higher plasma frequency nearer the surface for both temperatures, thus indicating the existence of electron accumulation near the surface.

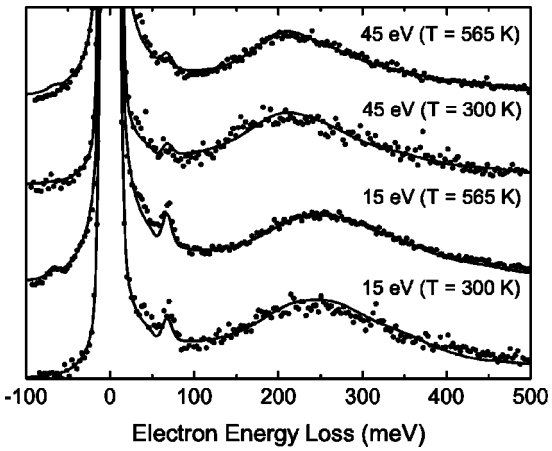

FIG. 1. Specular HREEL spectra recorded at 295 K and 565 K from an atomic hydrogen cleaned InN(0001)-(1×1) surface with incident electron energies of 15 and 45 eV (points) and the corresponding semiclassical dielectric theory simulations (solid lines).

HREELS simulations are calculated using a wave-vector-dependent dielectric function.[21,22] A five-layer model was used to simulate the HREEL spectra recorded at each temperature. The individual layer properties are summarized in Table I for both temperatures and show slight differences between the two models. Plasma dead layers of 3 Å and 3.8 Å were required for 295 K and 565 K, respectively. For accumulation layers, a dead layer is required to account for the quantized nature of the electron wave functions. This reflects the effect of the potential barrier formed at the surface, resulting in a boundary condition on all the wave functions, which suppresses the carrier concentration near the surface.[10,23] The carrier concentration tends to zero over a length approximately equal to half the average de Broglie

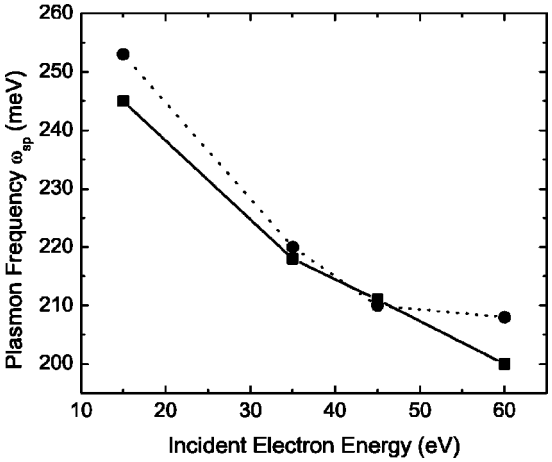

FIG. 2. The surface plasmon peak, ω_{sp}, energy-dispersion curves for both 295 K (solid line) and 565 K (dotted line). The plasmon peak positions were obtained from the HREEL spectra recorded from atomic hydrogen cleaned InN(0001)-(1×1) surface.

TABLE I. The plasma frequency profile used in the dielectric theory simulations of the HREEL spectra for both 295 K and 565 K.

Layer	1	2	3	4	5
			$T=295$ K		
d (Å)	3±0.5	3.5±0.5	8.0±1	25±2	∞
ω_p (meV)	0	446±10	328±2.5	248±1.5	192±1
			$T=565$ K		
d (Å)	3.8±0.5	6.0±0.5	8.0±1	25±2	∞
ω_p (meV)	0	415±10	328±2.5	254±1.5	192±1

wavelength of all the electron wave functions.[24] Three further layers of enhanced plasma frequency were needed to reproduce the plasmon tail at high loss energy. Finally, a bulk layer with a plasma frequency of 192 meV (for both temperatures) reproduced the plasmon peak position.

IV. THEORETICAL CALCULATIONS

In order to interpret the HREELS simulations for both temperatures, it is necessary to calculate the semiconductor statistics, that is, the plasma frequency and electron effective mass at the Fermi level as a function of the electron concentration. The two main parameters required to calculate the conduction-band dispersion are the band-edge effective mass, m_0^*, and the band gap, E_g.

The band gap of InN has been recently revised from the previously accepted value of 1.89 eV (Ref. 25) to the now accepted value of around 0.7 eV.[26–29] The revision in the band gap has been attributed to improvements in the quality of InN growth. Earlier growths of InN may have suffered from oxygen incorporation. Optical measurements have shown that the absorption edge blueshifts with increased oxygen incoporation, in some cases up to ~2–3 eV.[30] Additionally, the high carrier concentrations of most of the InN grown so far have inhibited the quantification of the fundamental band gap, due to the Burstein-Moss effect, which increases the energy of the optical transitions. At the same time, band renormalization shrinks the band gap, which further complicates the situation. In our work, the value reported by Wu *et al.* was used, with the $E_g(T=0\text{K})=0.69$ eV and the Varshni parameters, $\gamma=0.41$ meV/K and $\beta=454$ K.[12] This gives intrinsic band-gap values of 0.642 eV at 295 K and 0.561 eV at 565 K.

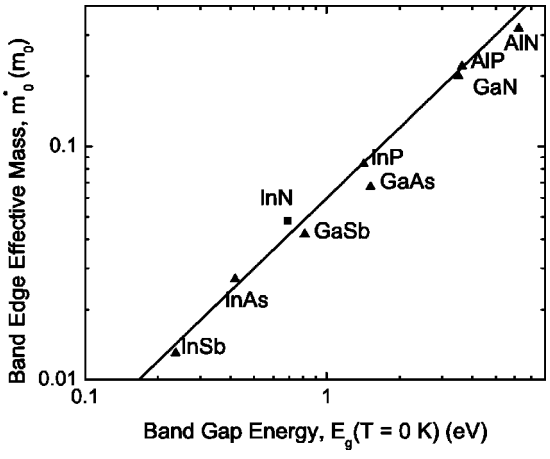

FIG. 3. The plot of the band-edge effective mass as a function of $E_g(T=0\text{ K})$ for a range of III–V materials (triangles), based on the values provided by Vurgaftman *et al.* (Ref. 31). The revised value for the effective mass is included (square).

The highly degenerate nature of the InN thin films grown so far has meant that there is still uncertainty over the value of the band-edge effective mass, m_0^*. Previous measurements of the effective mass, m^*, for heavily doped *n*-type hexagonal InN by Kasic *et al.*, estimated an isotropically averaged $m^*=0.14\ m_0$ from a combination of ellipsometry data analysis and Hall measurements.[32] Improvements in the crystalline quality of the material grown has resulted in a shift towards lower values of m^* being observed, with Wu *et al.* extrapolating their infrared reflection and Hall results to obtain a band-edge effective mass, m_0^*, of 0.07 m_0 at the bottom of the conduction band.[33] Recently, an effective mass of 0.042 m_0 has been successfully used as a parameter in simulations of photoluminescence spectra from InN.[34] In this work, $m_0^*=0.048\ m_0$ at T=0 K is used, based on the empirical relationship for semiconductors of $m_0^*\sim 0.07\ E_g$, as shown in Fig. 3.[35] The effective mass used for each temperature, along with the corresponding band gap, is shown in Table II.

An approximation of the two-band $\mathbf{k}\cdot\mathbf{p}$ model has been used to calculate the nonparabolic dispersion of the conduction band.[36] This model was modified for application in the high Fermi-level regime because of the high unintentional *n*-type doping. As mentioned previously, at these high carrier concentrations there are two competing effects: the Burstein-Moss effect and conduction-band renormalization. The Burstein-Moss effect refers to the shift towards larger optical transitions, as a result of band filling. The conduction-band renormalization arises from electron-electron and electron-impurity interactions.[33] These interactions result in the

TABLE II. The band-edge effective mass, m_0^*, for each temperature considered, based on the empirical relationship $m_0^*\sim 0.07\ E_g$ for III–V materials.

Temperature (K)	0	295	565
E_g (eV)	0.690	0.642	0.561
m_0^* (m_0)	0.0480	0.0446	0.0390

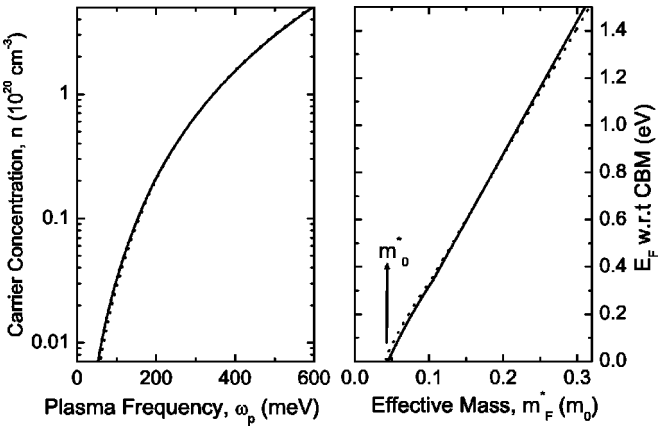

FIG. 4. The plot of the semiconductor statistics calculated using the two-band $\mathbf{k}\cdot\mathbf{p}$ model modified for the high Fermi-level regime, for both 295 K (solid lines) and 565 K (dotted lines). Both plots show little variation between the two temperatures. Finally, the band-edge effective mass, m_0^*, is highlighted and refers to the effective mass at $E_F=0$ eV. The values $m_0^*=0.0446\ m_0$ for 295 K and $m_0^*=0.0390\ m_0$ for 565 K were used for the calculations.

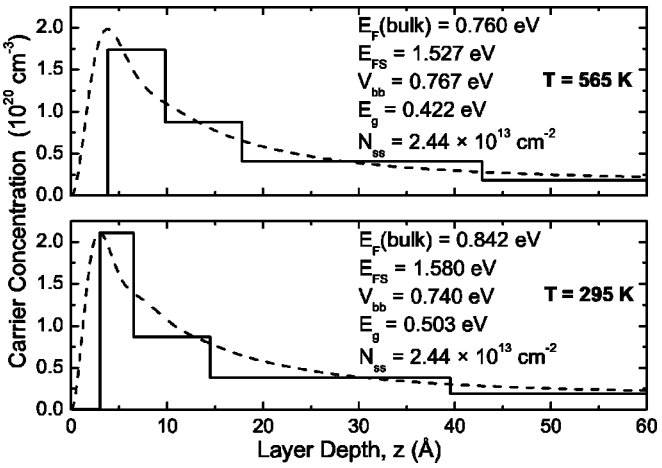

FIG. 5. The HREELS simulation layer profiles (solid lines) for 295 and 565 K, along with their carrier profiles (dashed lines) calculated by solving the Poisson equation within the MTFA. The corresponding bulk Fermi level, E_F(bulk), surface Fermi level, E_{FS}, band bending, V_{bb}, renormalized band gap, E_g, and surface state density, N_{SS}, for each temperature are also included.

shrinkage of the band gap, with a redshift of ~0.15 eV per decade of change of the carrier concentration beyond $\sim 10^{19}$ cm^{-3} being reported.[33] Since the $\mathbf{k}\cdot\mathbf{p}$ model was modified to account for band-gap renormalization, all subsequent references will be to the renormalized band gap rather than the intrinsic band gap.

The resulting conduction-band dispersion relation enabled the calculation of the semiconductor statistics, as described by Mahboob *et al.*[37] The calculated statistics are plotted in Fig. 4, and were used to translate the HREELS simulations into layer profiles of the space-charge region for the two temperatures. Figure 4 shows only a small difference between 295 K and 565 K.

Realistic smooth charge profiles were calculated by solving the Poisson equation within the modified Thomas-Fermi approximation (MTFA).[4,38] This allows nonparabolicty to be incorporated in a straightforward manner compared to the complications associated with modifying the Schrödinger equation to include nonparabolicity. In the Poisson-MTFA method, the carrier concentration as a function of depth, $n(z)$, depends on the local Fermi level which is determined by the bulk Fermi level and the value of the potential, $V(z)$, which, in turn, is given by the solution to the Poisson equation.[4,16] The MTFA accounts for the quantized nature of the electron wave function, whereby the surface potential barrier reduces the carrier concentration to zero at the surface.

The smooth charge profiles, which most closely match the HREELS simulation layer profiles are shown in Fig. 5 for both temperatures. The calculations reveal that the surface-state density and surface Fermi level are constant for the two temperatures, with $\sim 2.4\times 10^{13}$ cm^{-2} and ~1.5 eV, respectively. The surface Fermi level can be seen more clearly in Fig. 6. Figure 6 shows the Fermi level (E_F) conduction-band minimum (CBM), and the valence-band maximum (VBM) with respect to the VBM in the bulk, as a function of depth, for both temperatures. The surface Fermi level can be seen to be temperature invariant.

V. DISCUSSION

Surface accumulation was found to be present at both temperatures, as shown in Fig. 5. The carrier profiles of the near-surface region reveal a temperature invariant electron accumulation. The surface Fermi level with respect to the valence-band maximum and surface-state density calculated from the Poisson equation within the MTFA was found to be independent of temperature, yielding $\sim 1.5\pm 0.1$ eV and $2.4(\pm 0.2)\times 10^{13}$ cm^{-2}, respectively. These results are similar to previous measurements of the surface Fermi level[1] and surface-state density.[1,2,39] The band bending was found to be temperature invariant with $V_{bb}\sim 0.75$ eV for both 295 K and 565 K.

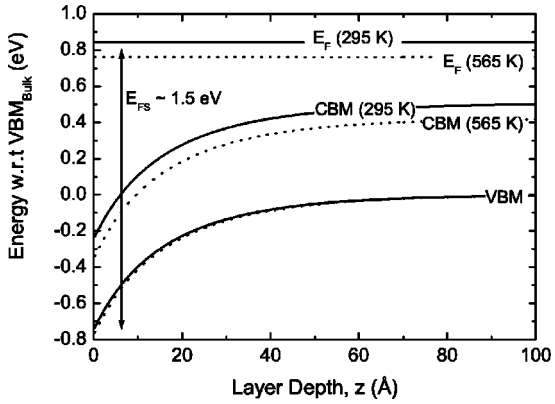

FIG. 6. The energy plot (that is the variation in the Fermi level, E_F, conduction-band minimum, CBM, and valence-band maximum, VBM, with respect to the VBM at the bulk) as a function of depth, z, for both 295 K (solid lines) and 565 K (dotted lines), calculated by solving the Poisson equation within the MTFA. The bulk VBM refers to the VBM where there is no band bending occurring i.e., $z\geqslant 90$ Å. The surface Fermi level is defined as the difference between the E_F and VBM at $z=0$ Å, which was found to be ~1.5 eV for both temperatures.

The temperature invariance of the near-surface region can be attributed to the small temperature dependence of the band gap. For narrow-gap semiconductors, the nonparabolicity of the conduction band determines many of the electronic properties, such as effective mass and density of states. By increasing the temperature, the band gap reduces and as a result the interaction between the conduction band and valence band increases. The increased interaction modifies the conduction-band curvature and the electronic properties change as a consequence. For InN, the change in the electronic properties with respect to temperature is small, as highlighted in Fig. 4. This can be attributed to the small reduction in the band gap with temperature compared to other narrow-gap semiconductors. For instance, the band gap of InN decreases by 19% as the temperature is increased from 0 to 565 K,[12] whereas in GaSb, which has a similar band gap to InN, the band gap decreases by 28% for the same change in temperature.[31]

The slightly broader HREELS simulation profile and corresponding Poisson-MTFA solution for 565 K compared to 295 K, observed in Fig. 5, is a consequence of a longer electron screening length. The charge profile width is determined by the screening length of the plasma formed by the conduction electrons. For degenerate semiconductors, the electron screening length is described by

$$\lambda_{\mathrm{TF}}^2 = \left(\frac{\pi}{6}\right)^{1/3} \frac{a_0^*}{4n^{1/3}}, \tag{1}$$

where λ_{TF} is the Thomas-Fermi screening length of the electron gas, n is the carrier concentration, and a_0^* is the effective Bohr radius, given by $a_0^* = \epsilon(0) a_0 / m_F^*$ with $\epsilon(0)$ the static dielectric constant, a_0 the Bohr radius, and m_F^* the effective mass at the Fermi level.[40] By varying the temperature, the screening length varies as a consequence of the change in the electron effective mass. For 565 K, the screening length is calculated to be 22.1 Å, compared to 21.6 Å for 295 K, resulting in a slightly broader HREELS simulation layer profile being required to simulate the high-temperature spectra, as shown in Fig. 5.

The maximum carrier concentration for the HREELS simulation layer profile is smaller for the higher temperature in Fig. 5. The carrier profile of the near-surface region is determined by the surface-state density, bulk carrier concentration, and the screening length of the electron gas. Since the surface-state density and bulk carrier concentration are temperature invariant, the amount of accumulating charge to ensure charge neutrality is also temperature invariant. In order to compensate for the longer screening length at 565 K, the maximum accumulation in the carrier profiles for 565 K (for both the HREELS simulation layer profile and Poisson-MTFA solution) is lower than for 295 K, as shown in Fig. 5.

VI. CONCLUSION

Electron energy-loss spectroscopy of the conduction band plasma excitations has been used to investigate the charge accumulation at the clean InN(0001) surface. It has been shown that the accumulation is temperature-independent with only a slight difference in the charge profiles observed. The slightly broader carrier profile observed at 565 K compared to 295 K can be accounted for by the change in the electron screening length as a consequence of the change in electron effective mass with temperature.

*Electronic address: C.F.McConville@warwick.ac.uk

[1] I. Mahboob, T. D. Veal, C. F. McConville, H. Lu, and W. J. Schaff, Phys. Rev. Lett. **92**, 036804 (2004).
[2] H. Lu, W. J. Schaff, L. F. Eastman, and C. E. Stutz, Appl. Phys. Lett. **82**, 1736 (2003).
[3] F. Bechstedt, J. Furthmüller, M. Ferhat, L. K. Teles, L. M. R. Scolfaro, J. R. Leite, V. Y. Davydov, O. Ambacher, and R. Goldhahn, Phys. Status Solidi A **195**, 628 (2003).
[4] I. Mahboob, T. D. Veal, L. F. J. Piper, C. F. McConville, H. Lu, W. J. Schaff, J. Furthmüller, and F. Bechstedt, Phys. Rev. B **69**, 201307(R) (2004).
[5] J. Tersoff, Phys. Rev. Lett. **52**, 465 (1984).
[6] J. Tersoff, Phys. Rev. B **32**, 6968 (1985).
[7] H. Lu, W. J. Schaff, L. F. Eastman, J. Wu, W. Walukiewicz, D. C. Look, and R. J. Molnar, Mater. Res. Soc. Symp. Proc. **743**, L4.10.1 (2003).
[8] C. H. Swartz, R. P. Tomkins, N. C. Giles, T. H. Myers, H. Lu, W. J. Schaff, and L. F. Eastman, J. Cryst. Growth **269**, 29 (2004).
[9] T. D. Veal and C. F. McConville, Phys. Rev. B **64**, 085311 (2001).
[10] M. Noguchi, K. Hirakawa, and T. Ikoma, Phys. Rev. Lett. **66**, 2243 (1991).
[11] Y. Chen, J. C. Hermanson, and G. J. Lapeyre, Phys. Rev. B **39**, 12 682 (1989).
[12] J. Wu, W. Walukiewicz, W. Shan, K. M. Yu, J. W. Ager III, S. X. Li, E. E. Haller, H. Lu, and W. J. Schaff, J. Appl. Phys. **94**, 4457 (2003).
[13] W. Walukiewicz, Physica E (Amsterdam) **20**, 300 (2004).
[14] H. Lu, W. J. Schaff, J. Hwang, H. Wu, W. Yeo, A. Pharkya, and L. F. Eastman, Appl. Phys. Lett. **77**, 2548 (2000).
[15] M. Walker, T. D. Veal, H. Lu, W. J. Schaff, and C. F. McConville, Phys. Status Solidi C (to be published).
[16] M. J. Lowe, T. D. Veal, A. P. Mowbray, and C. F. McConville, Surf. Sci. **544**, 320 (2003).
[17] E. J. Petit, F. Houzay, and J. M. Moison, Surf. Sci. **269–270**, 902 (1992).
[18] R. Fuchs and K. L. Kliewer, Phys. Rev. **140**, A2076 (1965).
[19] T. D. Veal, Ph.D. thesis, University of Warwick (2002).
[20] T. S. Jones, M. O. Schweitzer, N. V. Richardson, G. R. Bell, and C. F. McConville, Phys. Rev. B **51**, 17 675 (1995).
[21] Ph. Lambin, J. P. Vigneron, and A. A. Lucas, Comput. Phys. Commun. **60**, 351 (1990).
[22] Ph. Lambin, J. P. Vigneron, and A. A. Lucas, Phys. Rev. B **32**, 8203 (1985).
[23] D. H. Ehlers and D. L. Mills, Phys. Rev. B **36**, 1051 (1987).
[24] G. R. Bell, C. F. McConville, and T. S. Jones, Phys. Rev. B **54**,

2654 (1996).
[25] T. L. Tansley and C. P. Foley, J. Appl. Phys. **59**, 3241 (1986).
[26] S. X. Li, J. Wu, E. E. Haller, W. Walukiewicz, W. Shan, H. Lu, and W. J. Schaff, Appl. Phys. Lett. **83**, 4963 (2003).
[27] T. Inushima, M. Higasiwaki, and T. Matsui, Phys. Rev. B **68**, 235204 (2003).
[28] M. Higashiwaki, T. Inushima, and T. Matsui, Phys. Status Solidi B **240**, 417 (2003).
[29] J. Wu, W. Walukiewicz, K. M. Yu, J. W. Ager III, E. E. Haller, H. Lu, and W. J. Schaff, Phys. Status Solidi B **240**, 412 (2003).
[30] E. Kurimoto, M. Hangyo, H. Harima, M. Yoshimoto, T. Yamaguchi, T. Araki, Y. Nanishi, and K. Kisoda, Appl. Phys. Lett. **84**, 212 (2004).
[31] I. Vurgaftman, J. R. Meyer, and L. R. Ram-Mohan, J. Appl. Phys. **89**, 5815 (2001).
[32] A. Kasic, M. Schubert, Y. Saito, Y. Nanishi, and G. Wagner, Phys. Rev. B **65**, 115206 (2002).
[33] J. Wu, W. Walukiewicz, W. Shan, K. M. Yu, J. W. Ager III, E. E. Haller, H. Lu, and W. J. Schaff, Phys. Rev. B **66**, 201403(R) (2002).
[34] B. Arnaudov, T. Paskova, P. P. Paskov, B. Magnusson, E. Valcheva, B. Monemar, H. Lu, W. J. Schaff, H. Amano, and I. Akasaki, Phys. Rev. B **69**, 115216 (2004).
[35] B. R. Nag, Phys. Status Solidi B **237**, R1 (2003).
[36] E. O. Kane, J. Phys. Chem. Solids **1**, 249 (1957).
[37] I. Mahboob, T. D. Veal, and C. F. McConville, Appl. Phys. Lett. **83**, 2169 (2003).
[38] H. Übensee, G. Paasch, J. P. Zöllner, and S. Handschack, Phys. Status Solidi B **147**, 823 (1988).
[39] V. Cimalla *et al.*, Phys. Status Solidi C **0**, 2818 (2003).
[40] G. R. Bell, Ph.D. thesis, University of Warwick (1996).